Journal of Materials Chemistry C

Ionic Interactions Control the Modulus and Mechanical Properties of Molecular Ionic Composite Electrolytes

Journal:	*Journal of Materials Chemistry C*
Manuscript ID	TC-ART-08-2021-004119.R1
Article Type:	Paper
Date Submitted by the Author:	18-Oct-2021
Complete List of Authors:	Bostwick, Joshua; Penn State, Materials Science and Engineering Zanelotti, Curt; Virginia Polytechnic Institute and State University, Macromolecules Innovation Institue and Department of Chemistry Yu, Deyang; Virginia Polytechnic Institute and State University, Macromolecules Innovation Institue and Department of Chemistry Pietra, Nicholas; Virginia Polytechnic Institute and State University, Macromolecules Innovation Institue and Department of Chemistry Williams, Teague; Penn State, Materials Research Institute Madsen, Louis; Virginia Tech, Chemistry Colby, Ralph; Penn State, Materials Science and Engineering

Ionic Interactions Control the Modulus and Mechanical Properties of Molecular Ionic Composite Electrolytes

Joshua E. Bostwick,[1] Curt J. Zanelotti,[2] Deyang Yu,[2] Nicholas F. Pietra,[2] Teague A. Williams,[3] Louis A. Madsen,[2]* and Ralph H. Colby[1]*

[1]*Department of Materials Science and Engineering, Pennsylvania State University, University Park, Pennsylvania 16802, United States*

[2]*Department of Chemistry and Macromolecules Innovation Institute, Virginia Tech, Blacksburg, Virginia 24061, United States*

[3]*Materials Research Institute, Pennsylvania State University, University Park, Pennsylvania 16802, United States*

Abstract

Molecular ionic composites (MICs) are a new class of solid electrolytes that combine ionic liquids (ILs) and a rigid-rod double helical polyelectrolyte, poly(2,2′)-disulfonyl-4,4'benzidine terephthalamide (PBDT). In this study, we focus on the mechanical, dielectric, and ion diffusive dynamics of MICs with a fixed PBDT weight percent (10 wt%) and varying IL chemistry and molecular volume (V_m). All six MICs produce tensile moduli in the range of 50 – 500 MPa at 30 $^{\circ}$C, up to 60 x higher than the shear moduli of the same MICs. The high range of moduli and tensile: shear modulus ratio emphasizes that the distribution of PBDT chains and the strong ionic interactions between IL ions and PBDT chains dictate the modulus and the mechanical strength in MICs. Additionally, these MICs exhibit high ionic conductivities ranging from 1 – 6 mS cm^{-1} at 30 $^{\circ}$C consistent with the measured diffusion coefficients of the IL ions. The tunability of the extraordinary mechanical properties and high ionic conductivities of MIC electrolytes greatly inspire their use in advanced electrochemical devices.

Keywords:

Polymer electrolyte, ion gel, ionic liquid, rigid-rod polyelectrolyte, charge transport

Introduction

Polymer-based electrolytes have gained widespread interest due to their potential use in many electrochemical devices such as lithium-ion batteries,[1-5] fuel cells,[6-8] sensors,[9, 10] and actuators.[11-13] Tuning the component molecular structures can give rise to a wide variation and optimization of electrolyte properties for numerous applications, but often the ties between structure and properties remain ambiguous. Still, in many cases polymer-based electrolytes can be tailored to produce a combination of high conductivity, mechanical stiffness, and thermal stability.[14]

One strategy for producing desirable polymer-based electrolytes with these unique properties is through the incorporation of ionic liquids (ILs) into the polymer matrix.[15-18] ILs are molten salts with low melting temperatures that are safer than typical volatile solvents used in electrochemical applications due to their combination of negligible vapor pressure, a broad electrochemical window, high ionic conductivity, and thermal stability.[19] By combining ILs with polymers, the mechanical and conductive properties of these electrolytes are tunable through the selection of different polymers and ILs respectively. For example, Lodge et al. produced an IL-polymer based ion gel combining a triblock copolymer with 1-ethyl-3-methylimidazolium bis(trifluromethylsulfonyl) amide (EMIm-TFSA).[20] Through this combination, the ion gel produced a high mechanical toughness in the kJ m^{-3} range and stable mechanical strength in the kPa range at elevated temperatures while also producing an ionic conductivity 2/3 of that of the neat IL at room temperature.[20] Additionally, Watanabe et al. produced a series of ion gels combining 1-ethyl-3-methylimidazolium bis(trifluoromethanesulfonyl)imide (EMIm-TFSI) and poly(methyl methacrylate) and reached a maximum ionic conductivity of ~ 10^{-2} S cm^{-1} at room temperature.[21]

Recently, a new class of solid polymer electrolytes has emerged, dubbed molecular ionic composites (MICs) that combine the high ionic conductivity and electrochemical and thermal stability of ILs with the mechanical stiffness of a highly rigid sulfonated aramid, poly(2,2′-disulfonyl-4,4′-benzidine terephthalamide) (PBDT).[22-27] Typically, incorporating ILs into a polymer matrix lowers the mechanical strength as the IL weight percent (wt%) or temperature increases.[16, 28, 29] However, MICs are able to produce nearly temperature-independent tensile moduli into the GPa range[22, 23] as well as shear moduli in the MPa range[24, 25] while maintaining a high IL content of 75 – 90 wt%. This enables the MICs to have a high mechanical stiffness while also producing a high ionic conductivity and electrochemical stability over a wide temperature range. This interplay between the modulus and conductivity is adjustable in part due to the existence of a two-phase internal structure in MICs, (at less than 25 wt% PBDT), in which a polymer-rich "bundle" phase coexists with an IL-rich "puddle" or percolated fluid phase.[23, 24] The "bundle" phase creates a stiff and conductive electrostatic network driven by the collective (and individually weak) associative interactions among the PBDT rods and the IL ions[30] while the percolated fluid phase behaves simply as a neat IL due to the lack of PBDT rods within this phase. Recently, Yu et al. combined 10 wt% PBDT, 10 wt% lithium bis(trifluoromethanesulfonyl)imide (LiTFSI) salt, and 80 wt% 1-butyl-1-methylpyrrolidinium bis(trifluoromethanesulfonyl)imide (BMPyr-TFSI) IL to produce a MIC and implemented it in a lithium metal-based battery as a solid-state electrolyte. The battery produced stable cycling performance over a wide temperature range and maintained a 99% discharge capacity retention after 50 cycles at 150 ˚C.[25] Because of this unique combination of a high modulus and ionic conductivity, as well as their impressive preliminary battery performance over a wide temperature range, MICs are promising materials for future electrochemical devices and applications.

While previous studies have looked into the charge transport and modulus of MICs with a single IL and with varying PBDT wt%, it is still unknown how incorporating different ILs will impact these same properties in the MIC. Pal and Ghosh showed that producing ion gels with larger IL molecular volumes (V_m) led to a systematic decrease in the ionic conductivity and ionic diffusion as well as slower segmental motion of polymer chains over a wide temperature range.[31] Additionally, Likozar et al. showed that incorporating different ILs into a nitrile elastomer-based composite produced varying effects on the mechanical properties due to the interactions between the IL and the surrounding polymer matrix.[32] Because of these variable effects, it is important to understand how changing the IL V_m and chemical structure impacts the mechanical properties and charge transport in MICs in order for these solid electrolytes to be implemented for advanced electrochemical devices.

In this study, we analyze the mechanical, dielectric and diffusive responses of MIC electrolytes using six different ILs: 1-ethyl-3-methylimidazolium triflate (EMIm-TfO), 1-ethyl-3-butylimidazolium triflate (BMIm-TfO), 1-ethyl-3-butylimidazolium dicyanamide (BMIm-DCA), 1-ethyl-3-methylimidazolium bis(trifluoromethanesulfonyl)imide (EMIm-TFSI), 1-ethyl-3-butylimidazolium bis(trifluoromethanesulfonyl)imide (BMIm-TFSI), and 1-butyl-1-methylpyrrolidinium bis(trifluoromethanesulfonyl)imide (BMPyr-TFSI). We fabricated each MIC with 10 wt% PBDT and 90 wt% IL and compare their ionic conductivity, ion diffusion and glass transition temperature with those of their respective neat ILs. These properties were investigated using a combination of both uniaxial tensile analysis and linear viscoelasticity (LVE) for the mechanical response, dielectric relaxation spectroscopy (DRS), and NMR diffusometry. Probing the molecular dynamics of MICs with varying ILs allows for new understanding of the interactions between varying ILs at a fixed PBDT wt%, as well as how these different ILs affect the overall

mechanical, dielectric, and diffusive dynamics of MIC electrolytes. Additionally, by understanding how these properties vary with IL chemistry and V_m, we hope to gain further insight into how different MIC compositions can give rise to desired properties needed for the next generation of polymer electrolytes.

Experimental

Materials: Aqueous solutions of PBDT were produced by combining PBDT with Na^+ counterions and deionized water in vials. These solutions show a complete nematic liquid crystalline phase at ≥ 2.1 wt% PBDT. EMIm-TfO, BMIm-TfO, EMIm-TFSI, and BMIm-TFSI were purchased from Iolitec GmbH with purity > 99%. BMIm-DCA and BMPyr-TFSI were purchased from Solvionic with purity > 98%. **Figure 1** shows the structures of all the ILs used (with the IL V_m listed in Supporting Information **Table S1)** as well as PBDT with Na^+ counterions.

(a) BMIm-DCA **(b)** EMIm-TfO

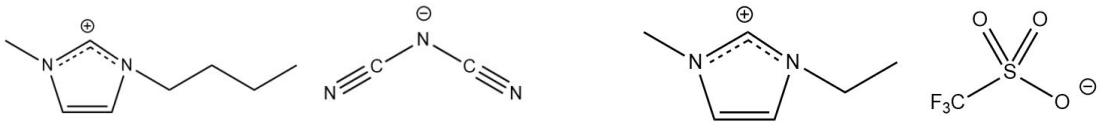

(c) BMIm-TfO **(d)** EMIm-TFSI

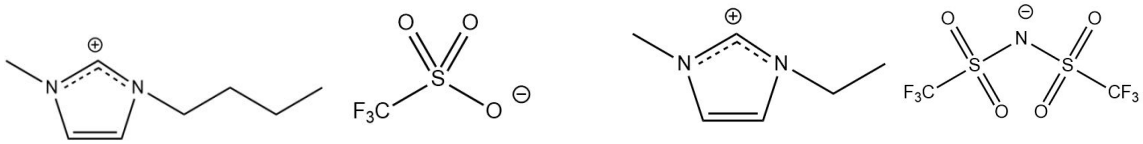

(e) BMIm-TFSI **(f)** BMPyr-TFSI

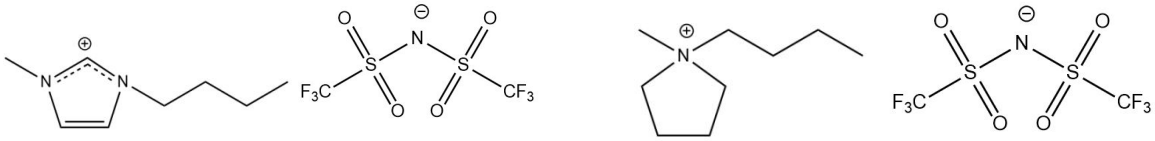

(g) Na-PBDT

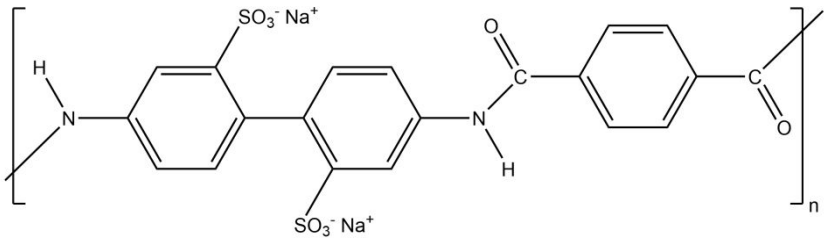

Figure 1: Molecular structures of the ILs, **(a)** BMIm-DCA **(b)** EMIm-TfO **(c)** BMIm-TfO **(d)** EMIm-TFSI **(e)** BMIm-TFSI **(f)** BMPyr-TFSI and **(g)** Na-PBDT. In total six ILs were combined with Na-PBDT to produce six MICs with 10 wt% PBDT.

MIC Film Preparation: MIC membranes that contained 10 wt% PBDT and 90 wt% of a desired IL were prepared using a solvent casting method as previously reported.[25, 27] For films with 100 – 200 μm thickness, 80 mg PBDT was dissolved in H_2O. For the chosen ILs that were hydrophilic, (BMIm-DCA and EMIm TfO) 720 mg of IL was also dissolved in H_2O. For films made from hydrophobic ILs, (the other four ILs) DMF was used to dissolve the IL. Both solutions, containing

PBDT and IL, were heated to 85 °C and then mixed together. The amount of solvent used to prepare each casting solution is summarized in **Table 1**. The casting solution was then equilibrated at 85 °C overnight. After equilibration, the casting solution was poured into a flat glass petri dish and dried at 85 °C overnight. The resulting self-standing dry MIC membrane was further dried under vacuum at 100 °C for two days and produced free-standing films with an example shown in **Figure 2**.

Figure 2: Image of the BMPyr-TFSI free standing film using 10 wt% PBDT and 90 wt% IL. Each film was controllably produced with a thickness of 100 – 200 μm, tailored to suit the needs of the characterization methods employed.

Table 1: Masses of PBDT, IL, and solvent used to prepare the casting solution for each MIC electrolyte film.

Sample	Mass of PBDT (mg)	Mass of IL (mg)	Mass of H_2O (g)	Mass of DMF (g)
BMIm-DCA	80.0	720	18.0	0
EMIm-TfO	80.0	720	16.0	0
BMIm-TfO	80.0	725	24.0	8.0
EMIm-TFSI	80.0	721	24.0	8.0
BMIm-TFSI	80.0	722	16.0	8.0
BMPyr-TFSI	80.0	721	8.0	8.0

Atomic Force Microscopy (AFM): AFM images of the MIC films were collected in tapping mode on a Bruker Dimension Icon system using an RTESP-300 Each MIC was secured to a glass substrate and the amplitude setpoint was adjusted to ensure a stable topography and good phase contrast (all MICs had a free air amplitude (FAA) ratio of roughly 0.75 – 0.9).

Differential Scanning Calorimetry (DSC): The glass transition temperature (T_g) of the ILs and MICs were determined using a TA Instruments DSC 2500. All samples were first heated to 200 °C and held isothermally for 5 min to remove any moisture absorbed during sample loading. All samples were then quenched from 200 °C to –150 °C at 100 °C min^{-1}. This is to prevent any of the ILs and MICs from crystallizing on cooling. Samples were then heated at 10 °C min^{-1} and the T_g was taken at the midpoint in the heat capacity change.

Mechanical Properties: Tensile stress-strain measurements were carried out using a TA Q800 dynamic mechanical analyzer. Prior to all measurements, the MICs were dried under vacuum at 80 °C for 24 h. After drying, the samples were loaded into a tension clamp and brought up to 30 °C where each film was equilibrated for 5 min. Once equilibrated, stress-strain measurements were carried out at a force ramp rate of 1 N min^{-1} until the sample broke. Each measurement was then repeated two more times with different cuts from the same film, resulting in three stress-strain curves for each MIC. Shear modulus measurements were carried out at 30 °C using a Rheometric Advanced Rheometric Expansion System (ARES)-LS1 rheometer with a transducer measuring 0.2 – 2000 g cm torque. All MICs were loaded onto 3 mm disposable aluminum plates and annealed in the rheometer for 1 h at 120 °C under dry nitrogen to insure proper contact with the plates. Once annealed, the sample was taken down to 30 °C where strain sweeps were taken at a frequency of 1 rad s^{-1} to determine the linear viscoelastic shear storage modulus.

Dielectric Relaxation Spectroscopy (DRS): Dielectric measurements of MICs and neat IL were carried out using a Novocontrol GmbH Concept 40 broadband dielectric spectrometer. All ILs were stored in a 40 ˚C vacuum oven. The 100 – 200 μm MIC films were pressed in between a polished 10 mm diameter top brass electrode and a polished 30 mm brass bottom electrode and placed under vacuum at 80 ˚C for 24 h for the MICs to enable adhesion of the MICs to the electrodes. Droplets of the ILs were placed onto a 30 mm brass electrode using a pipette and then sandwiched with a 10 mm brass electrode. The thickness of the ILs were maintained at 0.1 mm using silica spacers. The ILs were loaded into the Novocontrol and annealed at 100 ˚C under nitrogen for an hour to remove any moisture absorbed during sample loading while the MICs were annealed at 120 ˚C. Isothermal dielectric data were then collected using a sinusoidal voltage with an amplitude of 0.1 V over a frequency range of 10^{-1} – 10^{7} Hz. For the ILs, measurements were executed in steps of 5 ˚C in cooling from 100 ˚C to –100 ˚C followed by steps of 10 ˚C in heating from –100 ˚C to 100 ˚C while the MICs were measured in steps of 5 ˚C in cooling from 120 ˚C to –100 ˚C followed by steps of 10 ˚C in heating from –100 ˚C to 120 ˚C and steps of 5 ˚C from 120 ˚C to 200 ˚C.

NMR Diffusometry: The pulsed-gradient stimulated-echo sequence (PGSTE) was applied for all diffusion measurements from 0 to 150 ˚C. Self-diffusion coefficients of the IL ions were obtained from measuring the nuclei ^{1}H (cation diffusion) and ^{19}F or ^{13}C (anion diffusion). Before diffusion experiments, all samples were dried and sealed under vacuum to prevent water uptake. Diffusion measurements from 0 to 75 ˚C were performed using a 400 MHz Bruker Avance III WB NMR spectrometer equipped with a microimaging probe coupled to a Diff50 single-axis (z-axis) gradient system and a 5 mm ^{1}H rf coil. For IL anions that are not fluorinated, (DCA^{-}), a 5 mm ^{13}C rf coil was used. Diffusion measurements from 80 to 150 ˚C were performed using a 600 MHz Bruker

Avance III NMR spectrometer equipped with a DOTY 5 mm, Standard VT, 1H/X high gradient PFG probe. Under pulsed-field-gradient (PFG) NMR diffusometry, the Stejskal-Tanner equation was fit to the measured signal amplitude I as a function of gradient strength g,

$$I = I_0 e^{-D\gamma^2 g^2 \delta^2 \left(\Delta - \left(\frac{\delta}{3}\right)\right)} \quad \textbf{(1)}$$

where I_0 is the signal amplitude at $g = 0$, γ is the gyromagnetic ratio, δ is the effective gradient pulse duration, Δ is the diffusion time between gradient pulses, and D is the self-diffusion coefficient. The PGSTE sequence used with the Diff50 probe system (0 to 75 ˚C) used π/2 pulse lengths of 4.0, 5.2, and 8.1 μs for cation (^{1}H), anion (^{19}F), and anion (^{13}C), respectively. A repetition time of 0.50 s, a diffusion time of Δ = 30 ms, a gradient pulse length of δ = 1.4 ms, and acquisition times of 40 ms (cation) and 50 ms (anion) were used for cation and anion diffusion measurements. Maximum gradient strengths of 150 – 2300 G cm^{-1}, depending on temperature of experiment, were used to achieve 90% signal attenuation in sixteen steps. Sufficient signal-to-noise ratio (SNR) for each data point (> 10) was achieved by acquiring 128 and 64 scans for cation and anion (^{19}F), respectively. SNR for each (^{13}C) data point (>10) was achieved by acquiring 16 scans and 8192 scans, for the neat (DCA^-) IL and (DCA^-) MIC membranes.

The PGSTE sequence used with the DOTY probe system (80 to 150 ˚C) used π/2 pulse lengths of 4.1, 9.2, and 13.3 μs for cation (^{1}H), anion (^{19}F), and anion (^{13}C), respectively. A repetition time of 0.34 s, a diffusion time of Δ = 30 ms, a gradient pulse length of δ = 4.0 ms, and acquisition times of 100 ms (cation) and 120 ms (anion) were used for diffusion measurements. Maximum gradient strengths of 50 – 180 G cm^{-1}, depending on experimental temperature, were used to achieve 90% signal attenuation in sixteen steps. The same SNR procedure at low temperatures was used at high temperatures for both the ILs and MICs.

Results and Discussion

Morphology of MIC Electrolyte Films

Previous studies have shown that the morphology of IL-based composites can be determined through the topology and phase angle maps in atomic force microscopy (AFM).[23, 24, 33] Similarly, we employed AFM in tapping mode to explore the morphology of the varied IL MICs, all at a fixed PBDT content of 10 wt%. **Figure 3** shows the topological and phase angle maps of each MICs where we hypothesize the darker phase angles represent higher IL concentrated regions while the brighter phase angles represent the higher PBDT concentrated regions based on the height sensor scans. In each of these MICs, two distinct environments are present, corresponding to the PBDT-rich and IL-rich environments shown in previous studies at low PBDT concentration.[23, 24] The PBDT-rich environment corresponds to the PBDT rods and the IL ions forming associative "bundles" that enhance the stiffness of the MIC while the IL-rich environment represents the formation of IL "puddles" or percolated fluids where the IL ion motion is similar to that of the neat IL. While all of the MICs exhibit the two-phase environment, the internal structure of each of the MICs appears to be different depending on the IL incorporated into the PBDT matrix. Note that the phase contrast of the BMPyr-TFSI MIC is significantly darker than the other MICs. This is most likely due to IL leaking in atmospheric conditions, wetting the surface of the film and causing poor contact with the surface. However, the polymer fibrils are still shown in the height contrast images suggesting the two-phase environment exists in this MIC as well.

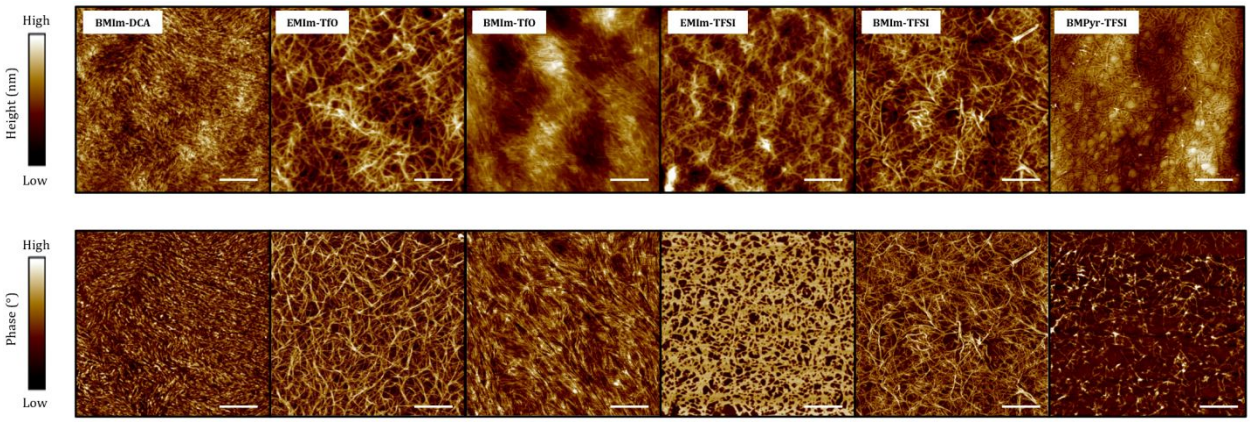

Figure 3: Atomic force microscopy (AFM) height (top) and phase angle (bottom) maps of the MICs with 10 wt% PBDT and 90 wt% ILs: The ILs for each MIC are listed in the topological image and the scale bar is listed at 400 nm for each image. Incorporating different ILs leads to different PBDT-IL interactions which likely drives the differences between the moduli in the MICs.

Analyzing the AFM images in **Figure 3**, we can determine an average MIC bundle diameter of approximately 14 ± 3 nm. Additionally, with a rod-rod spacing of 2.2 nm in a hexagonal lattice (based on volumetric estimates of initial and final material compositions and densities,[22] and MD calculations from Yu et al.[30]), we estimate that each bundle has approximately 40 ± 10 PBDT rods (**Figure 4** shows a schematic of the ideal cross-sectional area of a PBDT bundle on a microscopic scale) and that each MIC (with 10 wt% PBDT) has a volume fraction of bundles at approximately 50% while the volume fraction of percolated fluid is approximately 50% depending on the density of IL incorporated into the MIC. This is determined by taking a ratio between the volume fraction of PBDT rods that exist in the MIC (φ_{total}) and the volume fraction of PBDT rods that exist in a PBDT bundle (φ_{bundle}) Hence, at 10 wt% the percolated fluid phase that is essentially neat IL is certainly continuous and accounts for more to the high ionic conductivity discussed below. Note that these calculations of the bundle and percolated fluid volume fractions represent the rod-rod distance determined from MD simulations and not from previous X-ray scattering experiments that suggested that the rod-rod spacing between PBDT rods might be

smaller[22, 34] A smaller rod-rod spacing would indicate a larger value of PBDT rods per bundle and a smaller volume fraction of bundles in the overall MIC. Why the bundles have a constant diameter and number of PBDT rods is an interesting question that will be explored in a future study.

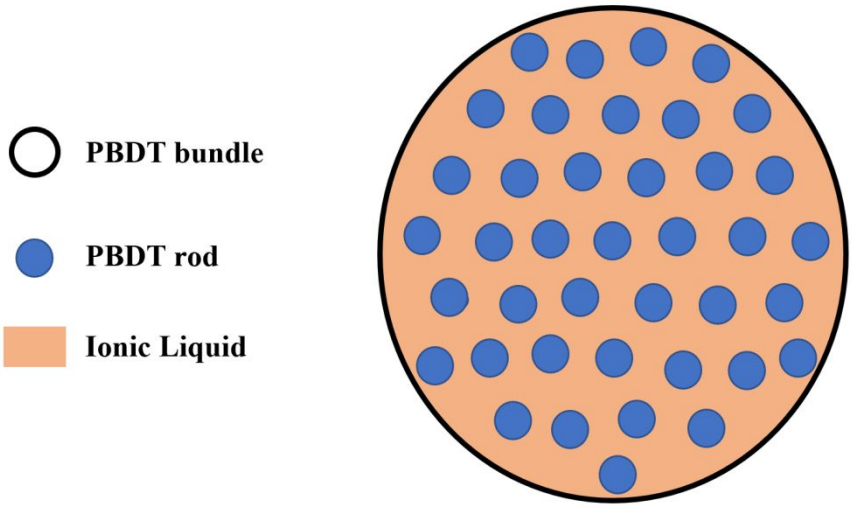

Figure 4: Idealized microscopic schematic of the cross-sectional area of a PBDT bundle. The bundle (dark circle), with diameter of approximately 14 nm, has approximately 40 PBDT rods (blue circles), packed in a quasi-hexagonal lattice with an approximate spacing of 2.2 nm. The remaining area is filled with IL (orange).

Mechanical Properties of MIC Electrolytes

To probe how the IL V_m and chemistry affects the mechanical properties of the MICs, we utilized a combination of tensile stress-strain measurements and linear viscoelasticity (LVE) in shear. **Figure 5** shows the uniaxial stress-strain curves for each of the MICs at 30 ˚C with the resulting Young's modulus (E), tensile strength, strain at break, and toughness for each MIC listed in **Table 2**.

From these measurements, three key factors are observed: (1) incorporating different ILs into the PBDT matrix leads to a wide range in E, from as low as 50 MPa in the BMIm-DCA MIC

to as high as 500 MPa in the EMIm-TFSI MIC, (2) larger IL anions with similar IL cations increase *E* in the MICs, (3) larger IL cations with similar IL anions decrease *E* in the MICs but increase the strain at break and the toughness. We hypothesize that the difference in *E* is due to the competing interactions between the IL cation, the IL anion, and the sulfonate groups from the PBDT in the PBDT-IL bundle phase. Increasing the IL anion V_m potentially lowers the interaction energy between the IL cation and IL anion in the bundle phase, allowing the alpha carbons from the IL cation to associate strongly with the sulfonate groups and strengthen the electrostatic network. This is portrayed in the $BMIm^+$ MICs where the smallest anion, DCA^- has the lowest *E* and increases up to 340 MPa when incorporating a much larger $TFSI^-$ anion. However, if we increase the IL cation V_m, the interaction energy between the sulfonate groups and the cation decreases, thus weaking the electrostatic network in the bundle phase and lowering *E* in the MICs. Other collective many-body ionic interactions might be at play that complicate this simple picture, and more systematic studies (including an array of simulations) will be needed to unravel more specific effects. Note though that while the strength of the electrostatic network changes depending on the IL incorporated, the modulus, tensile strength, and toughness are consistently higher than in other ion gels.[20, 35-38]

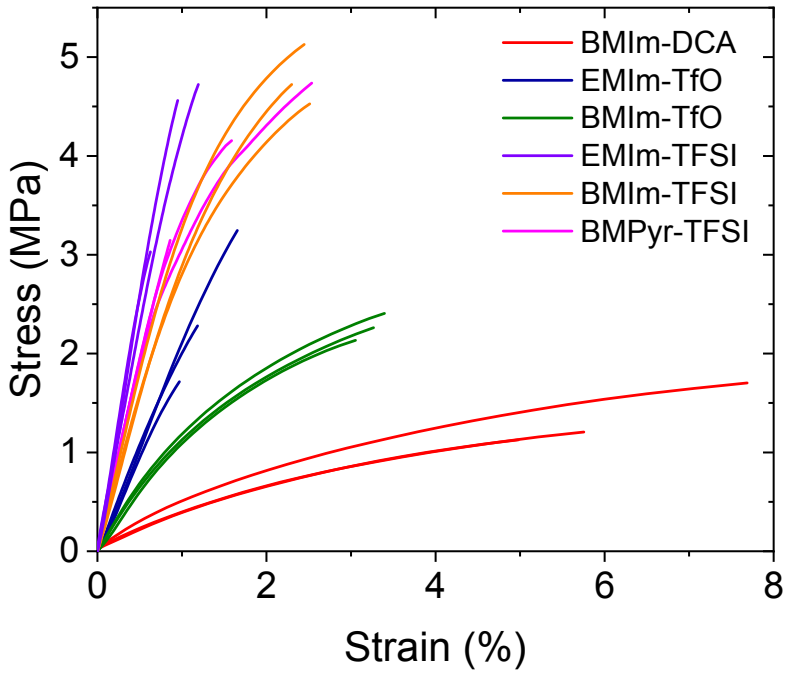

Figure 5: Uniaxial stress-strain curves of MIC films at a force ramp rate of 1 N min^{-1} at 30 ˚C. Measurements were repeated by cutting three test samples from each MIC film. The slope of the stress-strain curves at < 0.5% strain yields the Young's modulus (*E*) with values of *E*, tensile strength, strain at break, and toughness listed in **Table 2**. We hypothesize the differences in *E* are driven by the competing interactions between the IL cation, anion and sulfonate groups from the PBDT in the PBDT-IL bundle phase.

Table 2: Table of Young's modulus (*E*), tensile strength, strain at break, and toughness at 30 ˚C with standard deviations.

Sample	*E* (MPa)	Tensile Strength (MPa)	Strain at Break (%)	Toughness (MJ m^{-3})
BMIm-DCA	46 ± 8.0	1.3 ± 0.3	6.1 ± 1.4	5.5 ± 2.7
EMIm-TfO	210 ± 15	2.4 ± 0.8	1.3 ± 0.4	1.7 ± 1.0
BMIm-TfO	131 ± 10	2.3 ± 0.1	3.2 ± 0.2	4.6 ± 0.6
EMIm-TFSI	495 ± 48	4.1 ± 0.9	0.9 ± 0.3	2.1 ± 1.0
BMIm-TFSI	336 ± 27	4.8 ± 0.3	2.4 ± 0.1	7.4 ± 0.7
BMPyr-TFSI	398 ± 1.0	4.0 ± 0.8	1.7 ± 0.8	4.3 ± 3.0

To further explore the mechanical properties of MICs, we also compared the ratio of Young's moduli (*E*) and the shear moduli (*G*'). **Figure 6** shows the ratio of the tensile and shear

moduli (produced from frequency-independent strain sweeps in **Figure S1**) at 30 ˚C. All MICs exhibit *E* values surprisingly larger than their *G*' values, with *E*/*G*' ranging between 9 and 60. We hypothesize these varying ratios in the MICs is driven by two mechanisms: (1) the difference in the distribution of PBDT chain orientations between the shear plane and the tensile plane (anisotropy) and (2) the difference in the ionic interactions produced in the PBDT-IL bundle phase mentioned previously. Fox et al. used small-angle X-ray scattering (SAXS) on MICs with EMIm-TfO IL to show that the 2D scattering pattern of MICs is isotropic in the x-y plane (which in our case is the shear plane) regardless of PBDT wt%.[23] This means that when we study MICs through linear viscoelastic measurements, the PBDT chains axes are randomly distributed, producing a small range of *G*' from ~ 5 – 10 MPa over the entire IL V_m range. However, when the MICs are measured by SAXS in the y-z plane (the tensile plane) the 2D scattering pattern is highly anisotropic. In summary, the PBDT chains have a globally random alignment but are highly locally aligned in the film plane direction.[23] If the PBDT chains were to align along a single direction in the film plane, and if we were to measure the tensile modulus along that direction, then that *E* would likely be higher still.

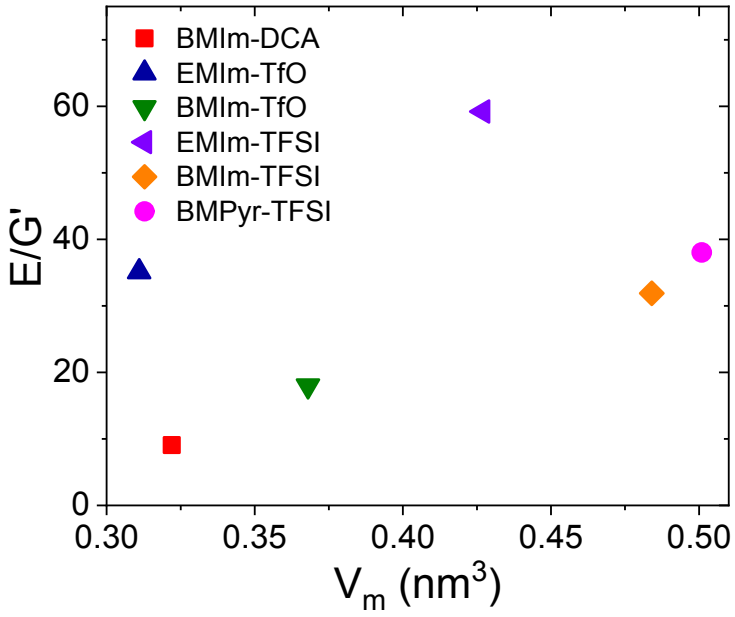

Figure 6: Ratio of the tensile and shear moduli of MICs as a function of IL molecular volume (V_m). Isotropic incompressible materials expect $E/G' = 3.0$ while MICs show $9 < E/G' < 60$. We suspect that the ratio differences in these moduli are due to the differences in the alignment distribution of PBDT chains in the tensile and shear planes as well as the differences in the specific ionic interactions in the PBDT-IL bundle phase. The two MICs formed using the smallest cation ($EMIm^+$) have large E/G' relative to the others, which generally show a trend of E/G' increasing with V_m.

Thermal Properties

We investigated the thermal properties of the ILs and their corresponding MICs through DSC (**Figure S2a and Figure S2b)**. In all MICs, the neat PBDT polymer does not exhibit any measurable thermal transitions detectable in DSC signifying that the thermal motions of the IL dictate both the glass transition temperature (T_g) and the melting temperature (T_m). While all the ILs show a distinct T_m, the majority of the MICs do not exhibit any T_m from the IL. We suggest that this is due to the confinement of the ILs among of the PBDT rods, which tend to prevent, or at least retard, crystallization.[23]

We also compared T_g between the neat ILs and their corresponding MIC (**Table 3**). All MICs exhibit a minimally higher T_g as compared to their corresponding IL ranging from 0 – 8 °C. When compared to the dynamic T_g determined from DRS, the difference between the two characterization techniques is only 5 °C. This suggests that while ion motion is slightly slower in the PBDT matrix, the MICs are still able to facilitate fast charge transport and T_g of the MICs is strongly correlated to the rearrangement of IL ions during charge transport.[39, 40]

Table 3: Glass transition temperature (T_g) comparison between DSC and DRS in the ILs and MICs.

	IL		MIC	
Sample	DSC[a] T_g (K)	DRS[b] T_g (K)	DSC[a] T_g (K)	DRS[b] T_g (K)
BMIm-DCA	181	180	181	186
EMIm-TfO	178	N/A	180	N/A
BMIm-TfO	190	N/A	190	N/A
EMIm-TFSI	180	N/A	185	183
BMIm-TFSI	185	180	190	185
BMPyr-TFSI	186	181	189	187

[a] T_g determined through DSC as the midpoint of the change in heat capacity on the second heating cycle. [b] T_g determined through DRS measurements defined where $\omega_{max}(T)$, at which the relaxation process in ε_{der} shows a frequency-dependent maximum, is extrapolated to $\omega_{max}(T_g) = 10^{-2}$ rad s^{-1} (determining the DRS T_g is further described in SI and shown in **Figure S3**). Samples with N/A DRS T_g values denote samples that were not measurable in the glassy state due to crystallization on cooling.

Ionic Conductivity

To investigate the influence of the IL V_m and chemical structure on the charge transport of MICs, we analyzed the ionic conductivity (σ_o) of both ILs and MICs in the regime where the imaginary part of the permittivity (ε") has a frequency-dependent power law of -1 (ω^{-1}) and σ_o is equivalent to $\omega\varepsilon_o\varepsilon$" where ω is the frequency and ε_o is the free space permittivity.[39, 41, 42] Shown in **Figure 7a** and **Figure 7b**, we fit the σ_o data using the Vogel-Fulcher-Tammann (VFT) equation,[43]

$$\sigma_o(T) = \sigma_\infty \exp\left(-\frac{BT_0}{T - T_0}\right) \quad \textbf{(2)}$$

where σ_∞ is the infinite temperature conductivity limit, B is a strength parameter proportional to fragility, and T_0 is the Vogel temperature (parameters listed in **Table S3**). Note that the data shown in **Figure 7a** and **Figure 7b** represent reproducible σ_o on heating and cooling. While some ILs and MICs crystallized on cooling, such as the TfO^- based systems, other ILs, such as the BMIm-DCA, BMIm-TFSI and BMPyr-TFSI ILs, only crystallized on heating, thus leaving gaps between the higher and lower temperature range.

While all MICs show lower σ_o compared to their corresponding IL, this ratio is never more than a factor of 3 at room temperature (**Figure S4**), suggesting that the interaction strength between the PBDT rods and the IL ions are decoupled from the charge transport in the MIC. Plotting σ_o as a function of V_m at 30 °C (**Figure 7c**) shows that all MICs achieve a σ_o greater than 1 mS cm^{-1}, maximizing at ~ 6 mS cm^{-1} in the BMIm-DCA MIC. This maximum in σ_o for the BMIm-DCA MIC could be due the non-spherical DCA^- structure, which promotes unfavorable packing between the ions.[44] Increasing V_m generally decreases the σ_o in the MICs due a decreased number density of charge carriers. Comparing IL structures, the σ_o is higher in the $EMIm^+$-based MICs than either the $BMIm^+$ or $BMPyr^+$-based MICs with similar cations. This is potentially due to the MICs with $EMIm^+$ IL cations having a higher molar concentration, allowing for higher molar conductivities (**Figure S5**).[45] Additionally, since the MICs have roughly a 50% percolated fluid phase, the interactions between the $EMIm^+$ cations and the IL anions from the neat IL are weaker relative to the larger IL cations, allowing for a larger fraction of IL charge carriers to contribute to the overall MIC conductivity from this phase. We discuss the relationship between the IL interactions and the ionic conductivity further below.

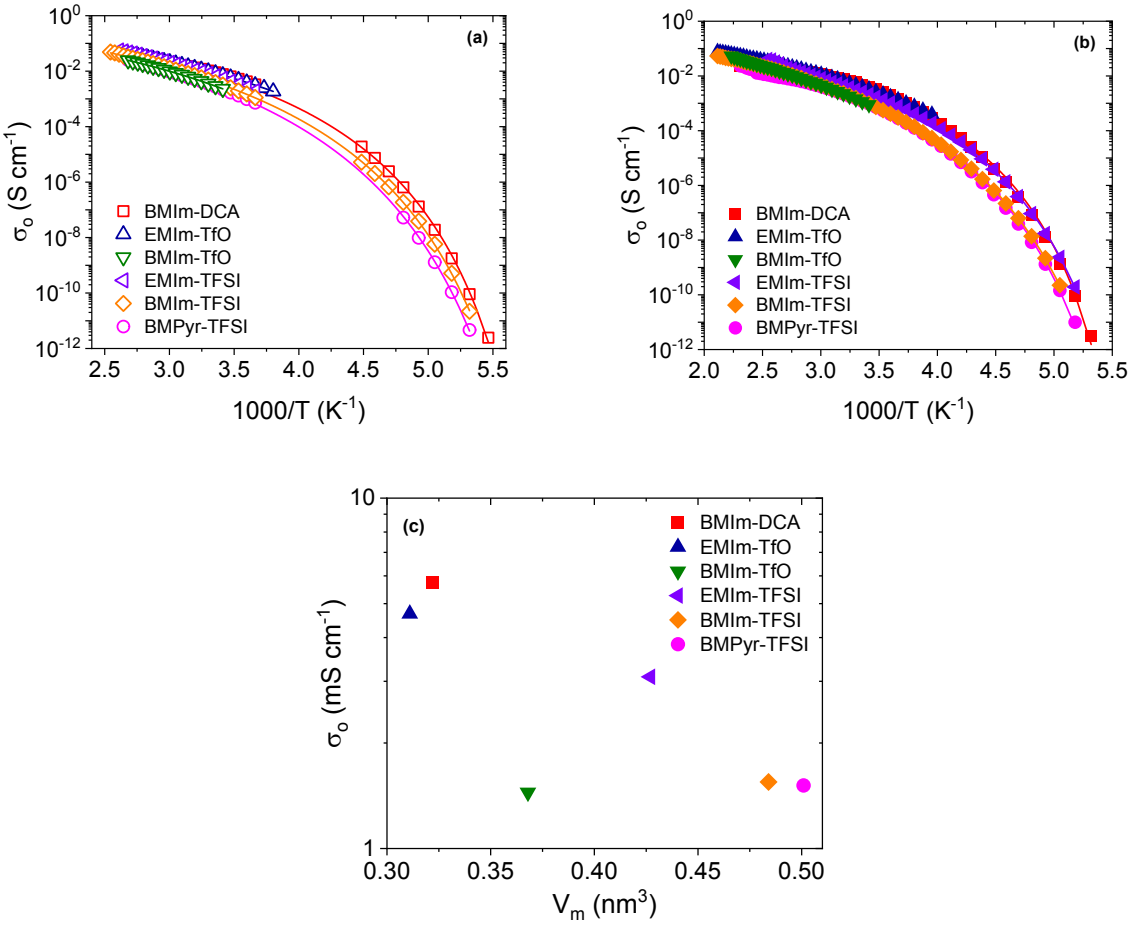

Figure 7: Temperature dependence of the ionic conductivity (σ_o) for **(a)** the neat ILs (open symbols) and **(b)** their respective 10 wt% PBDT MICs (filled symbols). All σ_o were fit with the VFT equation (**Eq. (2)**) (shown as colored lines) with the parameters listed in **Table S3**. **(c)** IL molecular volume (V_m) dependence of the MIC σ_o at 30 ˚C, showing a general trend of ionic conductivity decreasing as the V_m increases due to a decreased number density of charge carriers.

Comparing to a wide-array of other solid polymer-based electrolytes, MICs show a comparable or higher σ_o suggesting that MICs can provide the ionic conductivity necessary for practical electrochemical device applications.[46] We demonstrate this through **Figure 8** where we compare the ionic conductivity and the modulus (either G' or $E/3$) of the IL-dependent MICs and a wide variety of polymer electrolytes at 30 ˚C.[15, 28, 29, 47-51] Regardless of mechanical measurement implemented, LVE for the shear modulus or tensile tests for the Young's modulus, MICs boast both a simultaneously high ionic conductivity and modulus and outperform other polymer

electrolyte materials such as ion gels, single-ion conducting polymers, and block copolymer electrolytes that could be used for electrochemical applications.

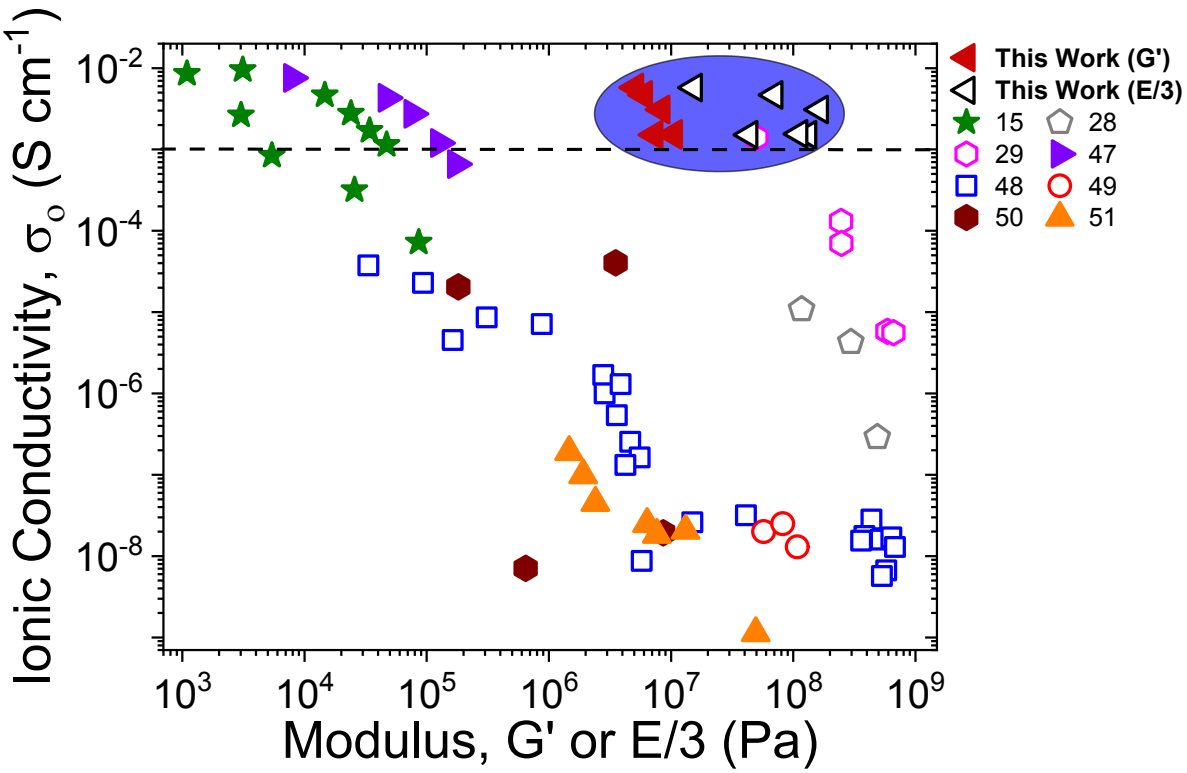

Figure 8: Relationship between the ionic conductivity (σ_o) and the modulus (either *G'* or *E/3*) for the MICs analyzed in this study and various polymer electrolytes including ion gels,[15, 28, 29, 47] single-ion conducting polymers,[48-50] and block copolymers[51] at 30 ˚C. Reference numbers are given in the figure legend where filled symbols represent materials with recorded shear moduli (*G'*) and open symbols represent materials with recorded tensile moduli (*E*). The dashed line represents the predicted ionic conductivity necessary for an ion conducting material to be properly implemented as a electrolyte for an electrochemical device, such as a battery.[46] The MICs (dark blue oval) show higher ionic conductivities and/or moduli than other ion conducting electrolytes emphasizing their potential as electrolytes in next-generation electrochemical devices.

Ionic Liquid Diffusion and MIC Ionicity

To further explore ion transport in ILs and MICs, we employed pulsed-field-gradient (PFG) NMR diffusometry to separately quantify the self-diffusion coefficients for the IL cations (^{1}H NMR) and IL anions (^{19}F and ^{13}C NMR). **Figure 9a**, **Figure 9b**, and **Figure 9c** show the cation

diffusion coefficients (D^+), anion diffusion coefficients (D^-) and the total diffusivity (D, the summation of the cation and anion diffusion coefficients) respectively for both the ILs and MICs. Note that we do not include the anion and the total diffusion coefficients for the BMIm-DCA MIC as the corresponding anion ^{13}C spectrum show poor resolution and signal-to-noise ratio (SNR). All MICs show D^+, D^-, and D that are comparable to, (within a factor of 3), their neat IL, paralleling the trends found from the ionic conductivity (σ_o) (**Figure S6)**. We suspect this arises from the ions' ability to rapidly diffuse in both the PBDT-IL bundle phase and in the percolated fluid phase.[22, 30, 52, 53] While one might expect that the IL cations in MICs to show much slower diffusion coefficients than the anions due to their associations with the sulfonate groups in the PBDT matrix, these ion associations are quite weak and only have a short lifetime (a few ns) on the fixed sulfonate groups.[30] This means that regardless of IL V_m, the IL ions are diffusing and exchanging with both PBDT-fixed sulfonate groups and mobile ions over this quick timescale, enabling fast ion transport in the MIC.

We fit the temperature-dependent cation, anion, and total diffusion coefficients using the VFT equation,

$$D_o(T) = D_\infty \exp\left(-\frac{BT_0}{T - T_0}\right) \quad \textbf{(3)}$$

where D_∞ is the diffusion at infinite temperature, B is a strength parameter and T_0 is the Vogel temperature (parameters listed in **Table S4**). For a proper comparison to the σ_o, the T_0 in the diffusion coefficients were fixed to the same T_0 found from σ_o. Using the same T_0 from the σ_o for each of the ILs and MICs led to good agreement with the diffusion data suggesting that σ_o and the ion diffusion processes strongly correlate with one another. We also compared the total MIC

diffusion coefficients from **Figure 9c** as a function of IL V_m at 30 ˚C in **Figure 9d**. Increasing the V_m drives a systematic decrease in the MIC diffusion, paralleling the trends found from σ_o.

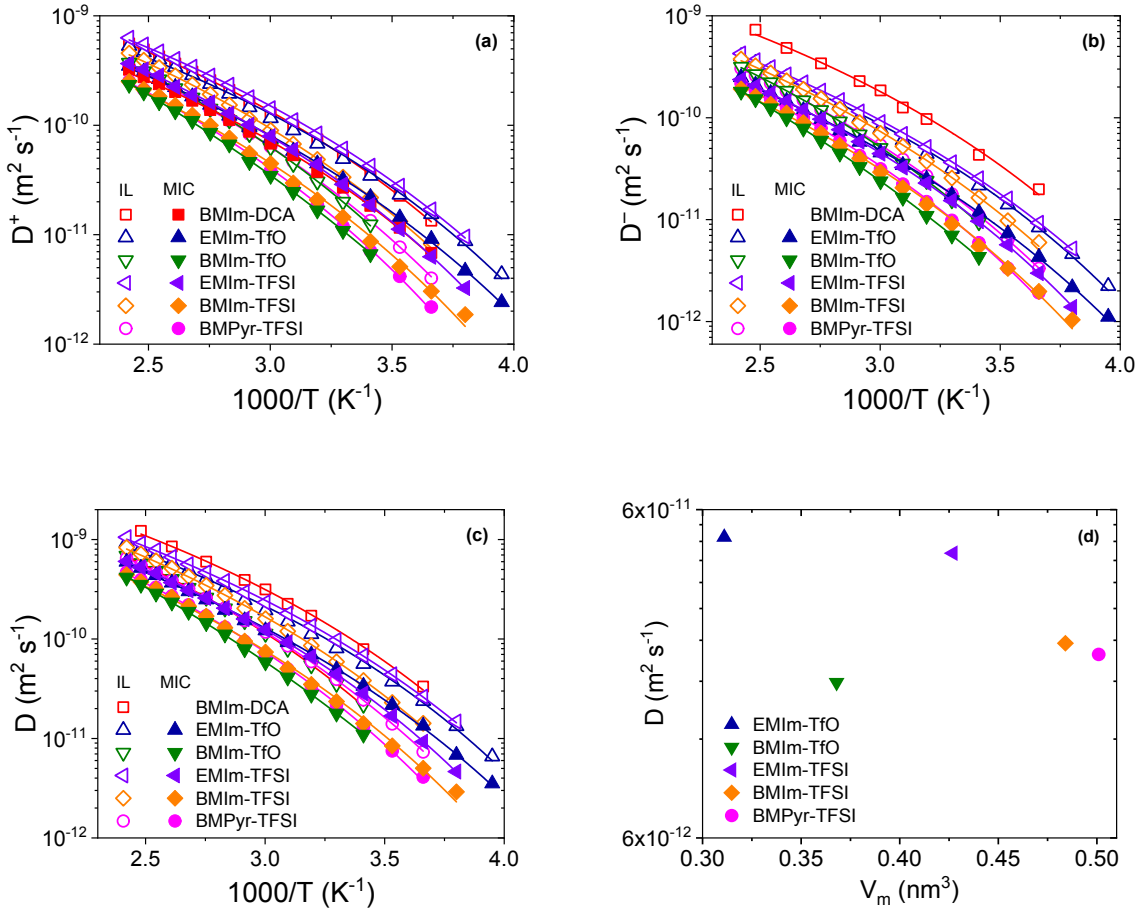

Figure 9: Temperature dependence of the **(a)** cation diffusion (D^+) **(b)** anion diffusion (D^-) and **(c)** diffusivity (D) for neat IL (open symbols) and MIC (filled symbols) samples. Solid lines are fits to the VFT equation (**Eq. (3)**) with parameters listed in **Table S4**. **(d)** IL molecular volume (V_m) dependence of the MIC diffusivity at 30 ˚C. Incorporating IL into the MIC slightly reduces the diffusion coefficient compared to the neat IL, indicating that ionic liquid in both the PBDT-rich and IL-rich regions remain mobile.

We further compared the effects of the ionic interactions with varying IL molecular volume and chemical structure for all the ILs and their corresponding MICs by comparing the diffusion coefficients with the ionic conductivity through the Nernst-Einstein equation[46]

$$\sigma_o = \frac{p_{IL} e^2}{H_R kT}(D^+ + D^-) \quad \textbf{(4)}$$

where p_{IL} is the number density of each IL, e is the elementary charge, H_R is the Haven ratio and kT is thermal energy. For the purpose of this study, this equation neglects the number density and diffusion coefficient of Na^+ counterions in the MIC from the PBDT chains. H_R represents the ratio between the predicted ionic conductivity based on the self-diffusion determined through NMR and the ionic conductivity determined through DRS.[54-56] This term is typically expressed through its inverse (H_R^{-1}) known as the ionicity which reaches a maximum value of 1.[57, 58] In systems where ion motions are correlated, ionicity is < 1, indicating that some fraction of ions exist in neutral clusters, such as ion pairs or quadrupoles. Therefore, the ionicity represents the fraction of ions that contribute directly to the conductivity where an ionicity of unity indicates that all charged species in the material have a net charge at all times. This is due to ionic conductivity measurements only being able to probe translational motions of ions that are pulled by the electric field while NMR diffusometry measurements can analyze the motions of all mobile ions.

Figure 10 shows the ionicity of both the ILs and their respective MICs. While both the ILs and MICs have H_R^{-1} values less than unity, both show completely different trends as the IL V_m increases. For the ILs, H_R^{-1} decreases as the cation alkyl chain length increases from an ethyl tail to a butyl tail. Watanabe et al. suggests this is due to the large contribution of intermolecular forces compared to the electrostatic interactions in the IL.[45] Increasing the hydrocarbon length leads to enhanced van der Walls interactions between the cations and these interactions dominate over the electrostatic attraction between the cation and anion in ILs. Further increasing the cation size with a $BMPyr^+$ structure leads to a slight increase in H_R^{-1} potentially due to the structures of aliphatic cations limiting close contacts with the anion because of steric hinderance.[59] However, when the size of the anion increases from TfO^- to $TFSI^-$, H_R^{-1} increases due to a more delocalized charge in

the $TFSI^-$ anion than in TfO^-. While the anionic charge in the $TFSI^-$ anion is well distributed in the sulfonyl groups, the TfO^- anionic charge is more localized, creating interactive sites with the IL cations.[60]

While the IL H_R^{-1} is dominated by the IL chemical structures, the MIC H_R^{-1} shows a slight increase (and likely non-significant) with increasing IL V_m, with all H_R^{-1} values ranging from 0.54 – 0.63. Comparing these values to the H_R^{-1} determined in a MIC with the same PBDT wt% and BMIm-BF_4 IL[24] shows that this H_R^{-1} agrees well with the H_R^{-1} produced in this study with the BMIm-BF_4 MIC producing a H_R^{-1} of roughly 0.6. Because of this, we propose that the H_R^{-1} of MICs is dominated by the change in PBDT concentration and the H_R^{-1} effects from the IL incorporated are minimal in this V_m range. Increasing the PBDT concentration has shown to increase H_R^{-1} close to unity potentially due to the formation of a near single PBDT-IL bundle-dominated phase with an enhanced static dielectric constant relative to its respective IL.[24]

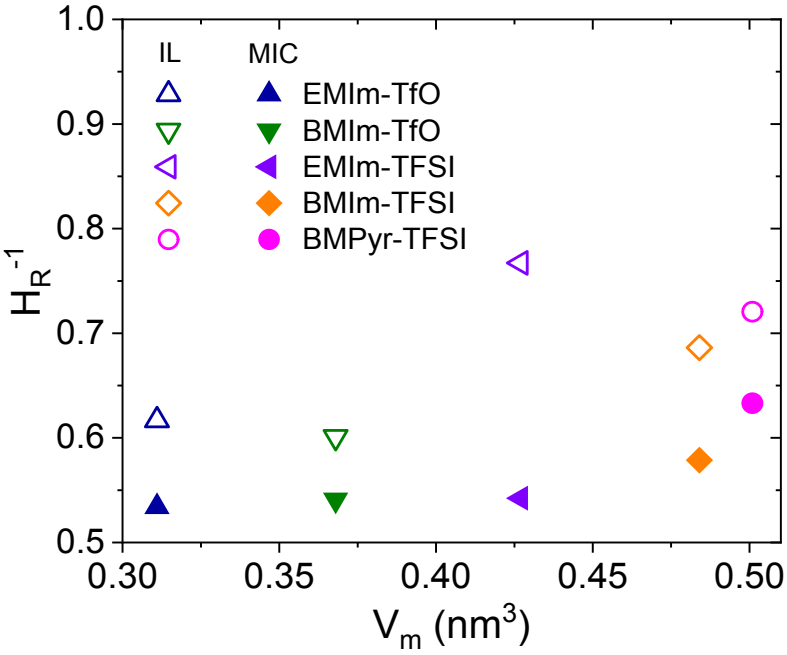

Figure 10: IL molecular volume (V_m) dependence of the ionicity (reciprocal of Haven ratio, H_R^{-1}) of the ILs and 10 wt% PBDT MIC films at 30 ˚C. All MICs produce an H_R^{-1} ranging from ~ 0.54 – 0.63 demonstrating that a fraction of diffusive IL ions does not contribute to the ionic conductivity. The ordering of IL ions among the PBDT rods appears to have a dominant effect on ionicity, as opposed to the IL chemical structure.

Conclusions

In this study, we compared the dielectric, diffusive and mechanical properties of molecular ionic composites (MICs) based on a combination of six different ionic liquids (ILs), each in turn, with 10 weight percent (wt%) of poly(2,2′-disulfonyl-4,4′-benzidine terephthalamide (PBDT). Combining the ILs with PBDT to form MICs led to Young's modulus (E) values between 50 – 500 MPa, a range that is 9 – 60 x higher than the shear modulus. We hypothesize this is due to two factors: (1) the differences in the PBDT chain alignment between the tensile and shear planes and (2) the competition between the sulfonate groups on the PBDT chain and the IL anion to interact with the IL cation in the PBDT-IL bundle phase that forms the mechanical matrix in MICs. Incorporating ILs with smaller alkyl cations apparently leads to stronger interactions with the

sulfonate groups and therefore, higher E. Larger IL anions led to weaker interactions with the IL cation, which may allow the cation to interact more readily with the sulfonate groups, further increasing E. Such observations suggest that using smaller cations, such as Li^+, and large anions, here $TFSI^-$, would be expected to increase the modulus even further. Preliminary results have shown that adding LiTFSI to an EMIm-TFSI-based MIC does increase the modulus but makes the resulting MICs extremely brittle at 30 wt% LiTFSI.

Thermal studies on the T_g showed a minimal increase between the MICs and their respective IL, as measured by DSC and DRS. The difference between the T_g calculated from DSC and DRS is within 5 ˚C between the two techniques strongly indicating that the low T_g in the MICs corresponds to the rearrangement of IL ions. Ionic conductivities in all MICs exhibit values greater than 1 mS cm^{-1} at 30 ˚C with the BMIm-DCA MIC achieving the highest conductivity at 6 mS cm^{-1}. All MICs exhibit a high ionic conductivity that is within a factor of 3 of the neat IL, suggesting that the charge transport is decoupled from any PBDT motions in the MIC.

NMR diffusometry illustrates that the diffusion of cations and anions in the neat IL and in MICs are comparable due to the short lifetime of associations between the fixed sulfonate groups on the PBDT chain and the IL ions. Relating ionic conductivity to diffusion through the ionicity (inverse Haven ratio, H_R^{-1}) shows only slight variations with IL type ($0.54 \leq H_R^{-1} \leq 0.63$) for MICs, with a slight increase in the ionicity at the highest IL molecular volumes studied.

By combining different ionic liquids with PBDT to form MIC electrolytes with widely varying properties, we have shown that MICs invariably have high ionic conductivity and highly tunable modulus and mechanical properties, with great promise for implementation into next generation electrolytes. These materials have ionic interactions controlling their mechanical

properties and this the usual tradeoffs, e.g., that an increase in modulus and/or strain at break accompanies a decrease in ionic conductivity.

Associated Content

Supporting Information

Ionic liquid molecular volume determination, determination of shear storage modulus, DSC traces of neat ILs and MICs, dielectric relaxations of ILs and MICs, VFT fitting parameters for the ionic conductivity, normalized room temperature ionic conductivity, molar conductivity of MICs, VFT fitting parameters for the ionic diffusion, normalized room temperature MIC diffusivity, ionic liquid and MIC ionicity.

Author Information

Corresponding Authors

***Email:** lmadsen@vt.edu (L.A.M)

***Email:** rhc@plmsc.psu.edu (R.H.C)

ORCID

Joshua E. Bostwick: 0000-0002-0640-5223

Curt J. Zanelotti: 0000-0003-2622-7345

Deyang Yu: 0000-0003-0587-1211

Louis A. Madsen: 0000-0003-4588-5183

Ralph H. Colby: 0000-0002-5492-6189

Conflicts of Interest

The authors declare no competing financial interest.

Acknowledgements

The authors would like to thank John Migliore for running DSC measurements as well as Theo J. Dingemans for providing the PBDT polymer. We are also very grateful for the support from the National Science Foundation under the DMR 1807934 and 1810194 awards.

References

1. W. H. Meyer, *Advanced Materials*, 1998, **10**, 439-448.
2. S.-J. Tan, X.-X. Zeng, Q. Ma, X.-W. Wu and Y.-G. Guo, *Electrochemical Energy Reviews*, 2018, **1**, 113-138.
3. H. Zhang, C. Li, M. Piszcz, E. Coya, T. Rojo, L. M. Rodriguez-Martinez, M. Armand and Z. Zhou, *Chemical Society Reviews*, 2017, **46**, 797-815.
4. L. Long, S. Wang, M. Xiao and Y. Meng, *Journal of Materials Chemistry A*, 2016, **4**, 10038-10069.
5. P. Yao, H. Yu, Z. Ding, Y. Liu, J. Lu, M. Lavorgna, J. Wu and X. Liu, *Frontiers in Chemistry*, 2019, **7**.
6. Y. Wang, K. S. Chen, J. Mishler, S. C. Cho and X. C. Adroher, *Applied Energy*, 2011, **88**, 981-1007.
7. R. Borup, J. Meyers, B. Pivovar, Y. S. Kim, R. Mukundan, N. Garland, D. Myers, M. Wilson, F. Garzon, D. Wood, P. Zelenay, K. More, K. Stroh, T. Zawodzinski, J. Boncella, J. E. McGrath, M. Inaba, K. Miyatake, M. Hori, K. Ota, Z. Ogumi, S. Miyata, A. Nishikata, Z. Siroma, Y. Uchimoto, K. Yasuda, K.-i. Kimijima and N. Iwashita, *Chemical Reviews*, 2007, **107**, 3904-3951.
8. C.-Y. Ahn, J. Ahn, S. Y. Kang, O.-H. Kim, D. W. Lee, J. H. Lee, J. G. Shim, C. H. Lee, Y.-H. Cho and Y.-E. Sung, *Science Advances*, 2020, **6**, eaaw0870.
9. F. Opekar and K. Štulík, *Analytica Chimica Acta*, 1999, **385**, 151-162.
10. V. K. Thakur, G. Ding, J. Ma, P. S. Lee and X. Lu, *Advanced Materials*, 2012, **24**, 4071-4096.
11. E. Margaretta, G. B. Fahs, D. L. Inglefield, C. Jangu, D. Wang, J. R. Heflin, R. B. Moore and T. E. Long, *ACS Applied Materials & Interfaces*, 2016, **8**, 1280-1288.
12. O. Kim, H. Kim, U. H. Choi and M. J. Park, *Nature Communications*, 2016, **7**, 13576.
13. A. A. Lee, R. H. Colby and A. A. Kornyshev, *Soft Matter*, 2013, **9**, 3767-3776.
14. T. P. Lodge, *Science*, 2008, **321**, 50.
15. S. Zhang, K. H. Lee, C. D. Frisbie and T. P. Lodge, *Macromolecules*, 2011, **44**, 940-949.
16. Y.-S. Ye, J. Rick and B.-J. Hwang, *Journal of Materials Chemistry A*, 2013, **1**, 2719-2743.

17. H. Wang, Z. Wang, J. Yang, C. Xu, Q. Zhang and Z. Peng, *Macromolecular Rapid Communications*, 2018, **39**, 1800246.
18. Y. Cao, T. G. Morrissey, E. Acome, S. I. Allec, B. M. Wong, C. Keplinger and C. Wang, *Advanced Materials*, 2017, **29**, 1605099.
19. Z. Lei, B. Chen, Y.-M. Koo and D. R. MacFarlane, *Chemical Reviews*, 2017, **117**, 6633-6635.
20. Y. Gu, S. Zhang, L. Martinetti, K. H. Lee, L. D. McIntosh, C. D. Frisbie and T. P. Lodge, *Journal of the American Chemical Society*, 2013, **135**, 9652-9655.
21. M. A. B. H. Susan, T. Kaneko, A. Noda and M. Watanabe, *Journal of the American Chemical Society*, 2005, **127**, 4976-4983.
22. Y. Wang, Y. Chen, J. Gao, H. G. Yoon, L. Jin, M. Forsyth, T. J. Dingemans and L. A. Madsen, *Advanced Materials*, 2016, **28**, 2571-2578.
23. R. J. Fox, D. Yu, M. Hegde, A. S. Kumbhar, L. A. Madsen and T. J. Dingemans, *ACS Applied Materials & Interfaces*, 2019, **11**, 40551-40563.
24. J. E. Bostwick, C. J. Zanelotti, C. Iacob, A. G. Korovich, L. A. Madsen and R. H. Colby, *Macromolecules*, 2020, **53**, 1405-1414.
25. D. Yu, X. Pan, J. E. Bostwick, C. J. Zanelotti, L. Mu, R. H. Colby, F. Lin and L. A. Madsen, *Advanced Energy Materials*, 2021, **11**, 2003559.
26. Y. Wang, C. J. Zanelotti, X. Wang, R. Kerr, L. Jin, W. H. Kan, T. J. Dingemans, M. Forsyth and L. A. Madsen, *Nature Materials*, 2021, DOI: 10.1038/s41563-021-00995-4.
27. D. Yu, C. J. Zanelotti, R. J. Fox, T. J. Dingemans and L. A. Madsen, *ACS Applied Energy Materials*, 2021, DOI: 10.1021/acsaem.0c03133.
28. A. Ito, T. Yasuda, T. Yoshioka, A. Yoshida, X. Li, K. Hashimoto, K. Nagai, M. Shibayama and M. Watanabe, *Macromolecules*, 2018, **51**, 7112-7120.
29. R. Mantravadi, P. R. Chinnam, D. A. Dikin and S. L. Wunder, *ACS Applied Materials & Interfaces*, 2016, **8**, 13426-13436.
30. Z. Yu, Y. He, Y. Wang, L. A. Madsen and R. Qiao, *Langmuir*, 2017, **33**, 322-331.
31. P. Pal and A. Ghosh, *Journal of Applied Physics*, 2019, **126**, 135102.
32. B. Likozar, *Soft Matter*, 2011, **7**, 970-977.
33. W. Fam, J. Mansouri, H. Li, J. Hou and V. Chen, *ACS Applied Materials & Interfaces*, 2018, **10**, 7389-7400.

34. Y. Wang, Y. He, Z. Yu, J. Gao, S. ten Brinck, C. Slebodnick, G. B. Fahs, C. J. Zanelotti, M. Hegde, R. B. Moore, B. Ensing, T. J. Dingemans, R. Qiao and L. A. Madsen, *Nature Communications*, 2019, **10**, 801.
35. L. Tao, Y. Liu, D. Wu, Q.-H. Wei, A. Taubert and Z. Xie, *Nanomaterials*, 2020, **10**, 2521.
36. H. Song, Z. Luo, H. Zhao, S. Luo, X. Wu, J. Gao and Z. Wang, *RSC Advances*, 2013, **3**, 11665-11675.
37. Z. Moshuqi, S. He, Y. Dai, J. Han, G. Huigan, J. Liu and M. Long, *ACS Sustainable Chemistry & Engineering*, 2018, **6**.
38. C. Shao, M. Wang, L. Meng, H. Chang, B. Wang, F. Xu, J. Yang and P. Wan, *Chemistry of Materials*, 2018, **30**, 3110-3121.
39. C. Krause, J. R. Sangoro, C. Iacob and F. Kremer, *The Journal of Physical Chemistry B*, 2010, **114**, 382-386.
40. J. R. Sangoro and F. Kremer, *Accounts of Chemical Research*, 2012, **45**, 525-532.
41. F. Kremer and A. Schönhals, *Broadband Dielectric Spectroscopy*, Springer, Berlin, Heidelberg, New York, 2003.
42. J. Leys, M. Wübbenhorst, C. P. Menon, R. Rajesh, J. Thoen, C. Glorieux, P. Nockemann, B. Thijs, K. Binnemans and S. Longuemart, *The Journal of Chemical Physics*, 2008, **128**, 064509.
43. L. Sun, O. Morales-Collazo, H. Xia and J. F. Brennecke, *The Journal of Physical Chemistry B*, 2016, **120**, 5767-5776.
44. Y. Zheng, Y. Zheng, Q. Wang and Z. Wang, *Journal of Chemical & Engineering Data*, 2021, **66**, 480-493.
45. H. Tokuda, K. Hayamizu, K. Ishii, M. A. B. H. Susan and M. Watanabe, *The Journal of Physical Chemistry B*, 2005, **109**, 6103-6110.
46. V. Bocharova and A. P. Sokolov, *Macromolecules*, 2020, **53**, 4141-4157.
47. B. Tang, S. P. White, C. D. Frisbie and T. P. Lodge, *Macromolecules*, 2015, **48**, 4942-4950.
48. J. F. Snyder, R. H. Carter and E. D. Wetzel, *Chemistry of Materials*, 2007, **19**, 3793-3801.

49. H.-S. Xu and C.-Z. Yang, *Journal of Polymer Science Part B: Polymer Physics*, 1995, **33**, 745-751.
50. S.-W. Wang and R. H. Colby, *Macromolecules*, 2018, **51**, 2767-2775.
51. J.-H. H. Wang, Doctoral Dissertation, Pennsylvania State University, 2015.
52. J. Hou, Z. Zhang and L. A. Madsen, *The Journal of Physical Chemistry B*, 2011, **115**, 4576-4582.
53. Z. Zhang and L. A. Madsen, *The Journal of Chemical Physics*, 2014, **140**, 084204.
54. N. H. LaFemina, Q. Chen, R. H. Colby and K. T. Mueller, *The Journal of Chemical Physics*, 2016, **145**, 114903.
55. N. H. LaFemina, Q. Chen, K. T. Mueller and R. H. Colby, *ACS Energy Letters*, 2016, **1**, 1179-1183.
56. G. E. Murch, *Solid State Ionics*, 1982, **7**, 177-198.
57. D. R. MacFarlane, M. Forsyth, E. I. Izgorodina, A. P. Abbott, G. Annat and K. Fraser, *Physical Chemistry Chemical Physics*, 2009, **11**, 4962-4967.
58. C. Gainaru, E. W. Stacy, V. Bocharova, M. Gobet, A. P. Holt, T. Saito, S. Greenbaum and A. P. Sokolov, *The Journal of Physical Chemistry B*, 2016, **120**, 11074-11083.
59. H. Tokuda, K. Ishii, M. A. B. H. Susan, S. Tsuzuki, K. Hayamizu and M. Watanabe, *The Journal of Physical Chemistry B*, 2006, **110**, 2833-2839.
60. H. Tokuda, K. Hayamizu, K. Ishii, M. A. B. H. Susan and M. Watanabe, *The Journal of Physical Chemistry B*, 2004, **108**, 16593-16600.